Supplementary Information

1.1 Neuroimaging data preprocessing

An overview of the neuroimaging data preprocessing pipeline is presented in Figure S1. Anatomical T1w scans and resting-state functional scans were preprocessed using the fMRIPrep workflow (1.4.1rc1; https://fmriprep.readthedocs.io/en/stable/; Esteban et al., 2019; RRID:SCR_016216) based on Nipype 1.2.0 (Gorgolewski et al., 2011; RRID:SCR_002502), which combines tools from multiple software packages. Many internal operations of fMRIPrep use Nilearn (RRID:SCR_001362), principally within the functional data preprocessing workflow.

Structural data preprocessing. Each structural image was visually inspected, and images affected by severe motion artifacts were excluded. T1w images were corrected for intensity nonuniformity (INU) with N4BiasFieldCorrection v2.1.0 (Tustison et al., 2010), distributed with ANTs 2.2.0 (Avants et al., 2008; RRID:SCR_004757). The INU-corrected T1w image was used as a T1w-reference image throughout the workflow. When several T1w images were available for the same participant, a T1w-reference image was computed by co-registering and averaging the INU-corrected T1w images using mri_robust_template (FreeSurfer 6.0.1, Dale et al., 1999). When three or more T1w images were available, an unbiased T1w template equidistant from all T1w images was generated. The T1w-reference image was then skull-stripped with a Nipype implementation of the antsBrainExtraction.sh v2.1.0 workflow (ANTs), using OASIS30ANTs as target template.

The skull-stripped T1w reference image was then segmented into cerebrospinal fluid (CSF), white matter (WM), and gray matter (GM) using FAST (FSL 5.0.9, RRID:SCR_002823, Zhang et al., 2001). Brain surfaces were reconstructed using recon-all (FreeSurfer 6.0.1, RRID:SCR_001847, Dale et al., 1999). The brain mask initially generated using ANTs was refined with a custom variation of a method that reconciles ANTs-derived and FreeSurfer-derived segmentations of the cortical gray matter (RRID:SCR_002438, Klein et al., 2017). The T1w reference image was co-registered to a standard template in MNI space (ICBM 152 nonlinear asymmetrical template version 2009c, MNI152NLin2009cAsym; Fonov et al., 2009; RRID:SCR_008796) using nonlinear registration with antsRegistration (ANTs 2.2.0), using brain-extracted versions of both T1w reference and the standard template.

Functional data preprocessing. For each resting-state functional run, the following preprocessing was performed. First, a reference functional volume and its skull-stripped version were generated using a custom methodology of fMRIPrep. When non-steady-state volumes were detected, they were averaged and used as a reference due to their enhanced tissue contrast. Alternatively, the median of a motion-corrected subset of volumes was used as a functional reference image. Head-motion parameters with respect to the functional reference image (i.e., transformation matrices and six corresponding rotation and translation parameters) were estimated using six-degree-of-freedom registration in MCFLIRT (FSL 5.0.9, Jenkinson et al., 2002).

A deformation field to correct for susceptibility distortions was estimated based on fMRIPrep's fieldmap-less approach based on the ANTs symmetric normalization (SyN) technique. The deformation field is that resulting from co-registering the functional reference to the same-subject T1w-reference with its intensity inverted (Wang et al., 2017; Huntenburg, 2014). Registration was performed with antsRegistration (ANTs 2.2.0), regularized by constraining deformation to be nonzero only along the phase-encoding direction, and modulated with an average fieldmap template (Treiber et al., 2016). Based on the estimated susceptibility distortion, an unwarped functional reference image was calculated for a more accurate co-registration with the anatomical reference image. The functional reference image was then co-registered to the T1w reference image using bbregister (FreeSurfer) which implements boundary-based registration (Greve & Fischl, 2009). Co-registration was configured with nine degrees of freedom to account for distortions remaining in the functional reference.

The functional time-series were resampled onto their native space by applying a single, composite transform to correct for head-motion and susceptibility distortions, to generate a preprocessed functional run in native space. The functional time-series were also resampled into standard volume space (MNI152NLin2009cAsym space) and onto the fsaverage5 standard surface. All resamplings were performed with a single interpolation step by composing all the pertinent transformations (i.e., head-motion parameters, susceptibility distortion correction, and co-registrations to anatomical [EPI-to-T1w] and reference spaces [T1w-to-MNI]). Volumetric resampling was performed using antsApplyTransforms (ANTs v2.1.0), configured with Lanczos interpolation to minimize the smoothing effects of other kernels (Lanczos, 1964). Surface resampling was performed using mri_vol2surf (FreeSurfer), by sampling the cortical ribbon at six intervals and assigning the average to each vertex.

Estimation of confound timeseries. Several confounding timeseries were calculated based on the preprocessed functional data. Framewise displacement (FD) and average change in mean intensity between each pair of fMRI volumes (DVARS) were calculated using their implementations in Nipype, following the definitions by Power et al. (2014). The three global signals were extracted within the CSF, the WM, and the whole-brain masks. The confound time series derived from head motion estimates and global signals were expanded with the inclusion of temporal derivatives and quadratic terms for each (Satterthwaite et al., 2013).

Conversion to CIFTI format. We converted the anatomical and functional data outputs of the fMRIPrep preprocessing pipeline to the Connectivity Informatics Technology Initiative (CIFTI; https://www.nitrc.org/projects/cifti/) format, which is compatible with HCP tools and offers a number of advantages over traditional volume (e.g., NIFTI) and surface (e.g., GIFTI) formats (e.g., Coalson et al., 2018). For example, in CIFTI format, cortical gray matter which conforms best to 2D geometry is stored as surface vertices, whereas subcortical structures which have globular 3D morphology are stored as subcortical voxels (e.g., Glasser et al., 2013). In addition, in CIFTI format, high-resolution neuroimaging data can be condensed into a set of gray matter coordinates (i.e., cortical surface vertices and subcortical voxels collectively known as “grayordinates”), which allows for a more compact representation and smaller file size (e.g., ~200k voxels in a standard 2mm isotropic volume space vs. ~90k grayordinates in the standard CIFTI space).

To convert the preprocessed data to the CIFTI format, we used the fmriprep_ciftify BIDS-app (Dickie et al., 2019; https://github.com/edickie/ciftify). This tool was adapted from the HCP minimal preprocessing pipelines to convert legacy neuroimaging data that do not meet the HCP data acquisition standards to the formats compatible with HCP tools (Glasser et al., 2013). As part of the structural fmriprep_ciftify workflow (ciftify_recon_all): 1) FreeSurfer output surfaces were converted to GIFTI and CIFTI formats, and 2) the native cortical meshes were aligned and resampled to the standard 32k fs_LR mesh using the MSMSulc algorithm, which aligns surfaces based on sulcal anatomy (Robinson et al., 2018). The 32k fs_LR mesh is a bilaterally symmetrical standard surface mesh that consists of vertices spaced about 2 mm apart and is best suited for the low-resolution fMRI data (Glasser et al., 2013). T1w images and volumetric outputs of the FreeSurfer pipeline were nonlinearly co-registered to the MNI standard space using FSL’s FNIRT, which unlike the spatial normalization in fMRIPrep (using ANTs), generates less distortion and does not overfit to folding patterns (Dickie et al., 2019).

As part of the functional fmriprep_ciftify workflow (ciftify_subject_fmri), preprocessed functional runs in T1w volume space (NIFTI format) were projected onto each participant’s grayordinate space (CIFTI dense timeseries format). Resampling of cortical data was performed using a weighted, ribbon-constrained approach, using the cortical gray matter ribbon generated by FreeSurfer, after excluding excessively noisy voxels. Resampling of subcortical data was performed in a subcortical parcel-constrained manner using subcortical parcels which were generated by FreeSurfer segmentation. Surface (cortical vertices) and volumetric (subcortical voxels) timeseries in native space were mapped onto the standard grayordinate space (~32k

subcortical voxels and ~32k cortical vertices in each hemisphere). All subsequent denoising operations and analyses were performed on the functional data in CIFTI format.

1.2 Denoising of the resting-state functional data

Motion quantification. Head motion has been shown to artificially inflate functional connectivity estimates for short-distance connections and decrease functional connectivity estimates for long-distance connections (e.g., Power et al., 2012). For each functional run, we calculated two quality control measures related to head motion: framewise displacement (FD; Power et al., 2014), an index of head displacement between adjacent timepoints, and DVARS (Smyser et al., 2010), an index of change in global intensity between adjacent timepoints.

Following Burgess et al. (2016), DVARS were calculated on the minimally preprocessed CIFTI dense timeseries after intensity normalization to a global mean of 10,000. DVARS were then median centered to control for differences in thermal noise across participants, which have been linked to differences in head size (Burgess et al., 2016). For each functional run, we quantified contamination by head motion using the following measures: mean FD and number of timepoints contaminated by motion with FD > 0.39 mm and/or DVARS > 4.9 (Burgess et al., 2016). We excluded functional runs with < 4 minutes of data uncontaminated by motion (i.e., FD < 0.39 mm and DVARS < 4.9). This resulted in exclusion of 6 participants from the training dataset, such that the final sample used to train the normative models included 79 participants (M_{age} = 23.2, SD_{age} = 11.8, range: 6-45). No participants were excluded from the test dataset.

Denoising approach. To minimize the effects of head motion and other sources of noise and global artifacts on resting-state functional connectivity, we performed the following steps using custom Matlab code (MATLAB_R2019b). Resting-state functional data in CIFTI format, which had been minimally preprocessed using fMRIPrep, were intensity normalized to a global 4D mean of 10,000. We then built a general linear model with the following regressors: constant, linear, and quadratic terms, 6 head motion parameters and their squares, first-order temporal derivatives of the 6 motion parameters and their squares, mean tissue and global signals and their squares, first-order temporal derivatives of the mean tissue and global signals and their squares (e.g., Parkes et al., 2018). All regressors, with the exception of the constant, linear, and quadratic terms, were normalized prior to inclusion in the model. Variance associated with each of the 39 nuisance regressors was then regressed out of the minimally preprocessed and intensity-normalized resting-state fMRI data. Following nuisance regression, cleaned functional data were temporally filtered using a second-order zero-phase Butterworth filter with a high-pass cut-off frequency of 0.009 Hz (Burgess et al., 2016).

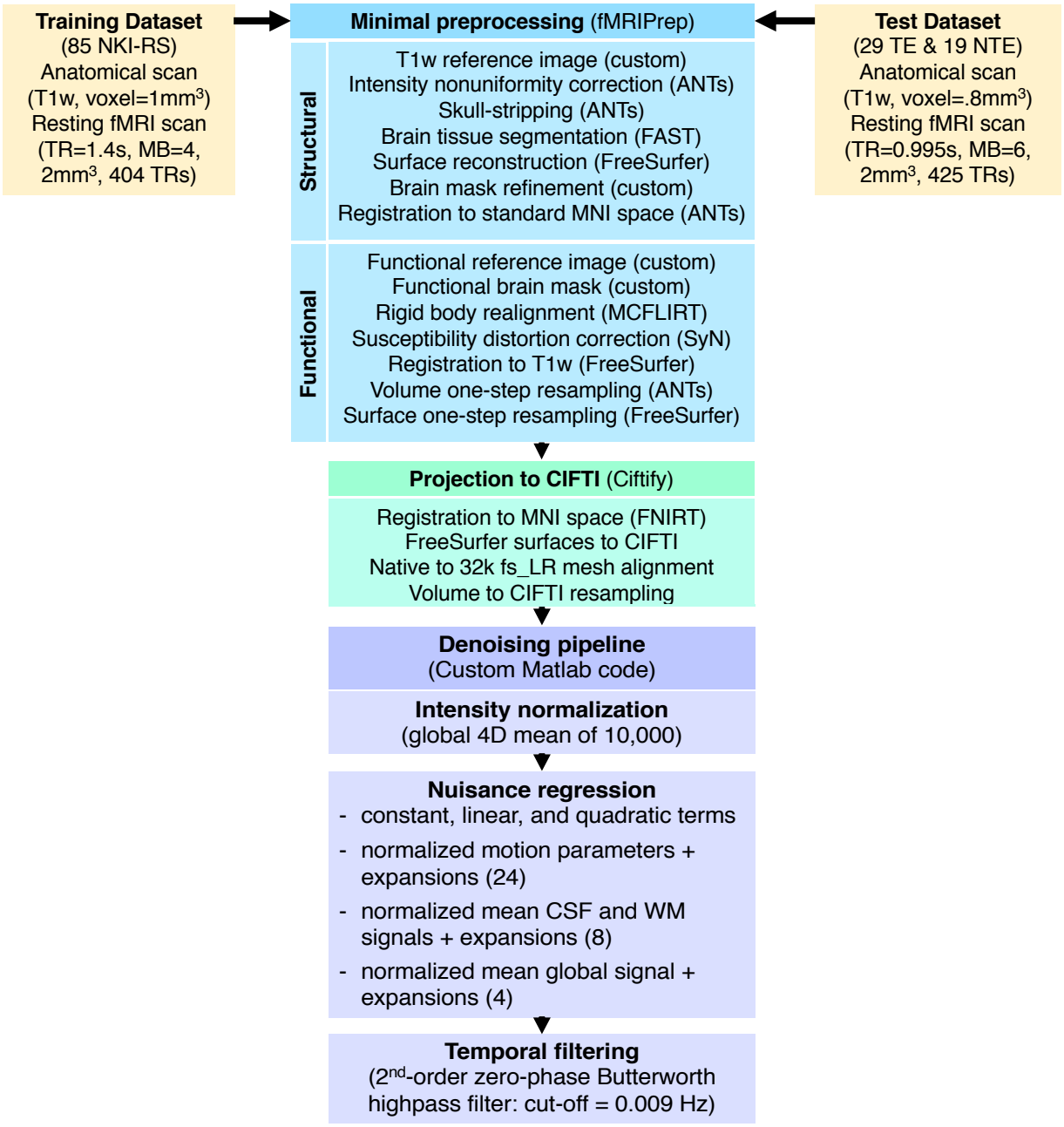

Figure S1. Overview of the preprocessing and denoising workflows.

1.3 Functional connectivity estimation

All functional connectivity estimation operations were performed on the cleaned and filtered functional data using custom Matlab code and Connectome Workbench v1.4.2 (https://www.humanconnectome.org/software/workbench-command). An overview of the functional connectivity estimation workflow is presented in Figure S8.

Parcellation scheme. We used the Cole-Anticevic Brain-wide Network Partition (CAB-NP v1.1) to parcellate the brain into 718 regions of interest (ROIs; 360 cortical and 358 subcortical) organized into 12 functional networks: primary visual, secondary visual, somatomotor, cingulo-opercular, dorsal attention, language, frontoparietal, auditory, default mode, posterior

multimodal, ventral multimodal, and orbito-affective (Ji et al., 2019; https://github.com/ColeLab/ColeAnticevicNetPartition; see Figure S2). This network partition was generated using the HCP's multimodal cortical parcellation atlas (HCP_MMP1.0; Glasser et al., 2016), which consists of 180 cortical parcels in each hemisphere. The network partition was further extended into subcortical gray matter by assigning each subcortical voxel to the cortical network with which it had the strongest average correlation (Ji et al., 2019).

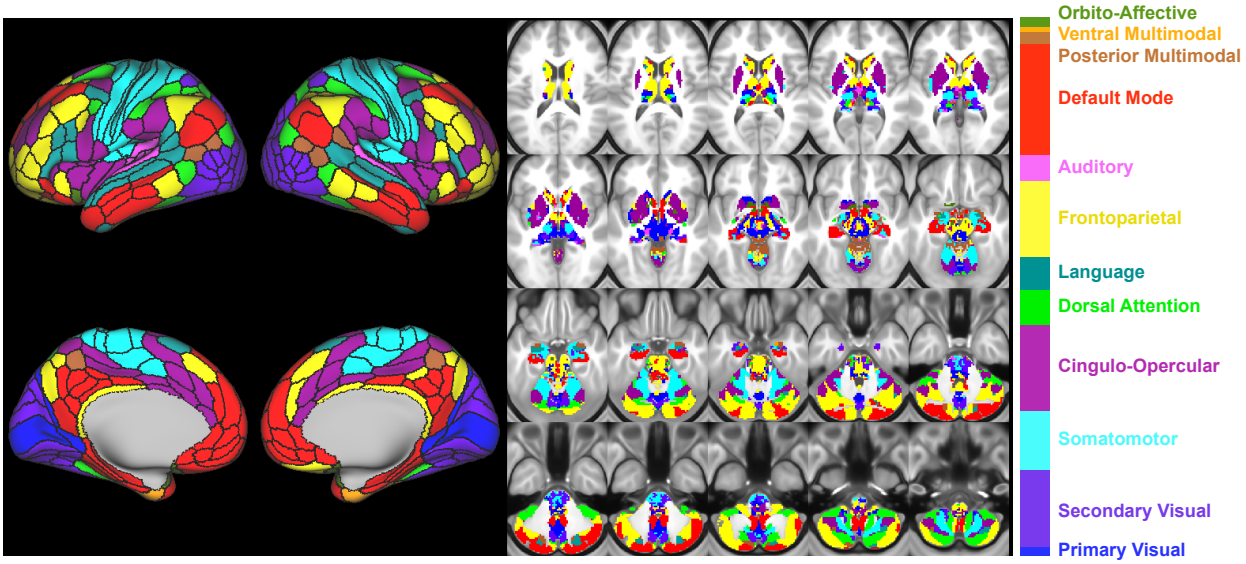

Figure S2. The Cole-Anticevic Brain-wide Network Partition (CAB-NP v1.1) was used to parcellate the brain into 360 cortical and 358 subcortical regions of interest organized into 12 functional networks.

We extracted mean timeseries from each of the 718 ROIs within the CAB-NP atlas using wb_command -cifti-parcellate. Prior to estimating functional connectivity between each pair of ROIs, we discarded the first eight timepoints to allow for magnetic equilibration. As a result, we used a total of 396 volumes for each participant in the training dataset and 417 volumes for each participant in the test dataset. For each participant in the training dataset, we calculated temporal signal-to-noise ratio (tSNR) for each of the 718 ROIs. We then created a group median tSNR map (see Figure S3) and excluded ROIs with median tSNR < 100 (151 ROIs; 21% of total ROIs). All excluded ROIs were subcortical and located either near the borders of the field-of-view or in the areas of EPI signal dropout.

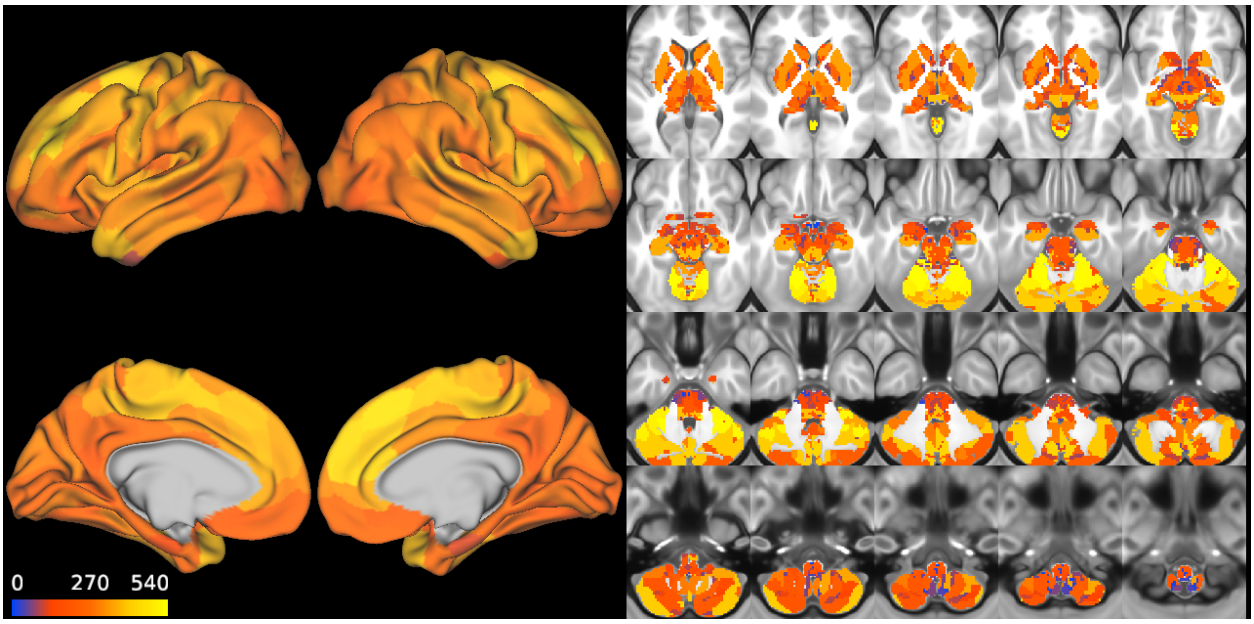

Figure S3. Group median temporal signal-to-noise ratio (tSNR) for each of the 718 ROIs in the Cole-Anticevic Brain-wide Network Partition atlas (CAB-NP v1.1). ROIs with median tSNR < 100 (purple-blue) were excluded from the analyses.

We used the remaining 567 ROIs to compute pairwise functional connectivity by calculating Pearson's correlation coefficients between each pair of ROIs. Correlation coefficients were then converted to Z-scores using Fisher's r-to-Z transformation. As a result, each participant had a 567 x 567 functional connectivity matrix (160,461 unique functional connections or edges) which was then used for estimation of functional brain maturity (see Figure S4).

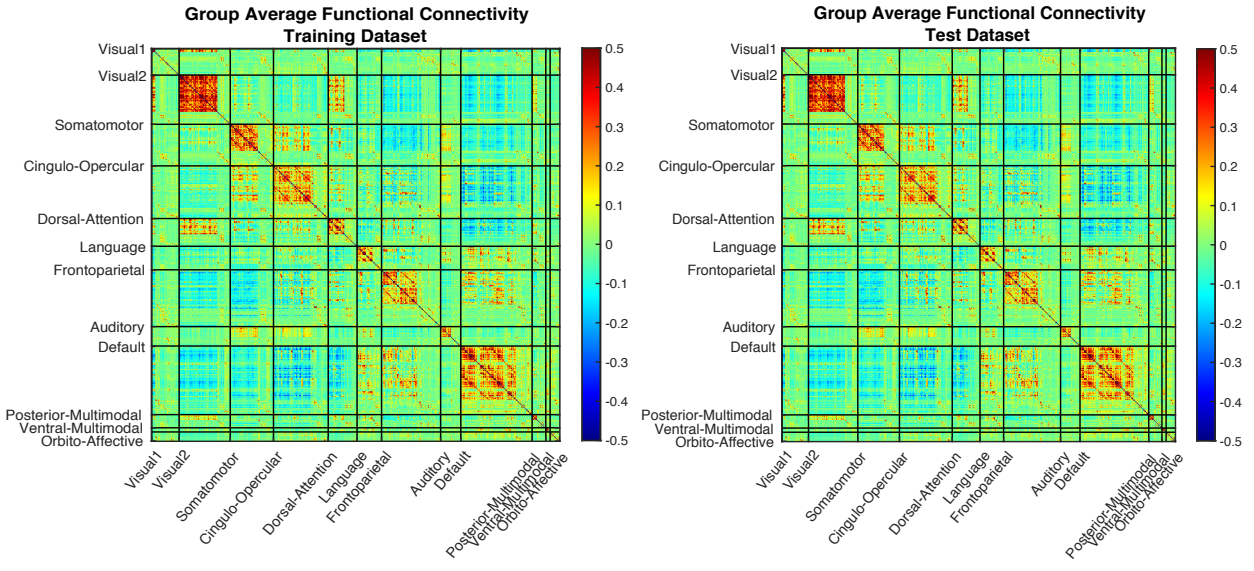

Figure S4. Group mean functional connectivity matrices for the training (left panel) and test (right panel) datasets.

Quality control. To determine whether our denoising approach was successful and estimate the amount of residual motion in the cleaned and filtered functional data, as well as its effects on functional connectivity, we performed the following quality control steps. We plotted the distributions of functional connectivity estimates (Fisher r-to-Z-transformed correlation coefficients) for the training and test datasets (see Figure S5). Consistent with the previously reported effects of global signal regression on functional connectivity (e.g., Ciric et al., 2017), both distributions of functional connectivity estimates were normal in shape and centered on zero.

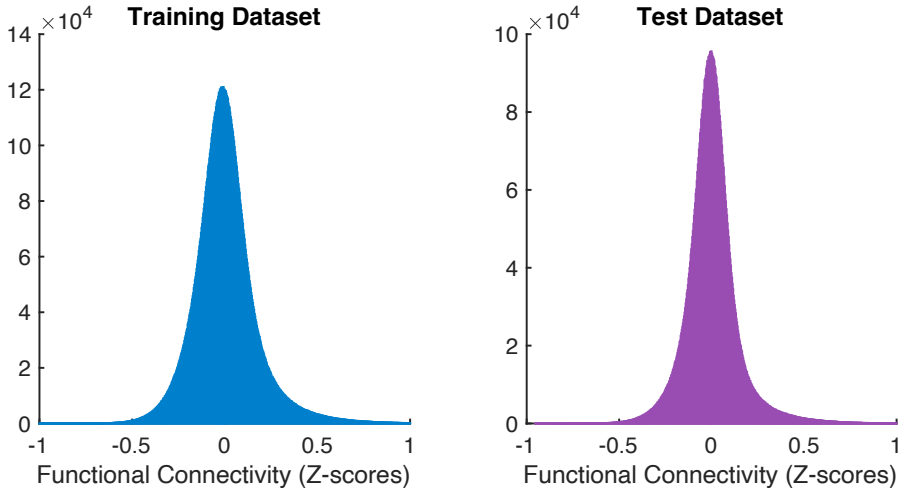

Figure S5. Distributions of functional connectivity estimates (Z-scores) in the training dataset (left panel) and the test dataset (right panel). Consistent with the previously reported effects of global signal regression (e.g., Ciric et al., 2017), both distributions of functional connectivity estimates were normal in shape and centered on zero.

In addition, we calculated correlations between each edge (i.e., functional connection between a given pair of ROIs) and mean FD in the training and test datasets (Figure S6). In the training dataset, 39% of edges were correlated with FD at uncorrected $p < 0.05$ and 28% of edges were correlated with FD at FDR-corrected $p < 0.05$. In the test dataset, 9% of edges were correlated with FD at uncorrected $p < 0.05$ and none were correlated with FD at FDR-corrected $p < 0.05$ (Figure S7). To minimize the effects of residual motion on functional connectivity estimates in the training dataset, we excluded edges that were correlated with FD at uncorrected $p < 0.05$ in the training dataset from all subsequent analyses. The same edges were also excluded from the test dataset.

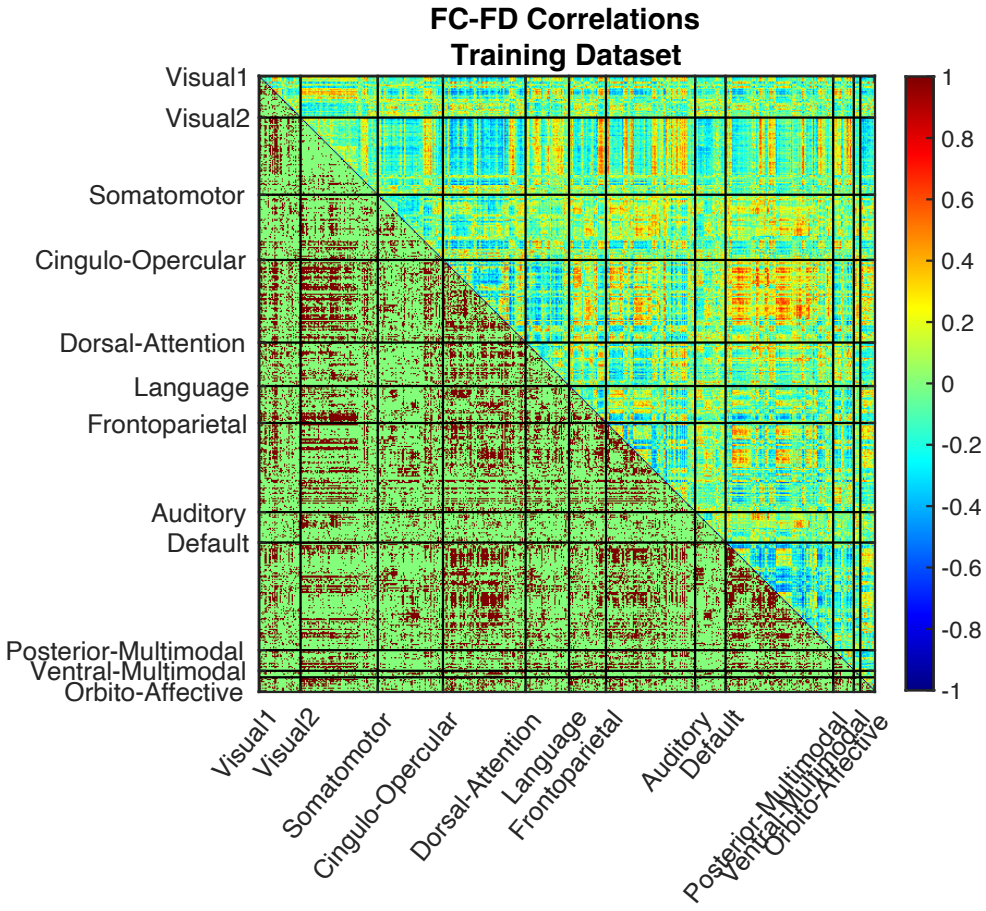

Figure S6. Correlations between functional connectivity (FC) estimates and mean framewise displacement (FD). The upper triangle of the matrix shows correlation coefficients, whereas the lower triangle shows statistical significance of the FC-FD correlations. In the lower triangle, edges that are correlated with FD below the FDR-corrected threshold of p = *0.05 are shown in brown, whereas edges that are not correlated with FD are shown in green. Functional connections correlated with FD below the uncorrected threshold of* p = *0.05 were excluded from subsequent analyses.*

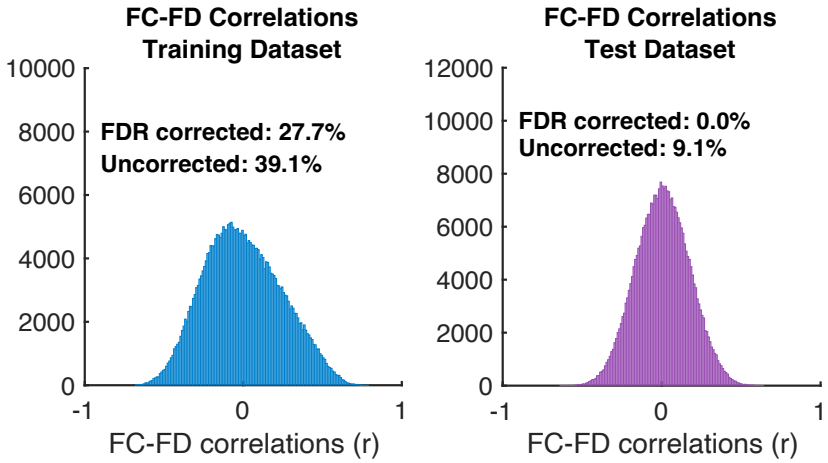

Figure S7. Distributions of correlation coefficients between functional connectivity (FC) estimates and mean framewise displacement (FD) in the training dataset (left panel) and the test dataset (right panel). In the training dataset, 39% of edges were correlated with FD at uncorrected p < *0.05 and 28% of edges were correlated with FD at FDR-corrected* p < *0.05. In the test dataset, 9% of edges were correlated with FD at uncorrected* p < *0.05 and none were correlated with FD at FDR-corrected* p < *0.05.*

1.4 Training the normative model of affective network maturation

We used machine learning to train the normative model of affective network maturation using the functional connectivity matrices of the selected NKI-RS participants as the training dataset and the functional connectivity matrices of the trauma-exposed participants as the test dataset. All machine learning operations were performed in Matlab R2019b using the Statistics and Machine Learning Toolbox and the Regression Learner App (Natick, Massachusetts, The MathWorks Inc.). An overview of the machine learning workflow is presented in Figure S8.

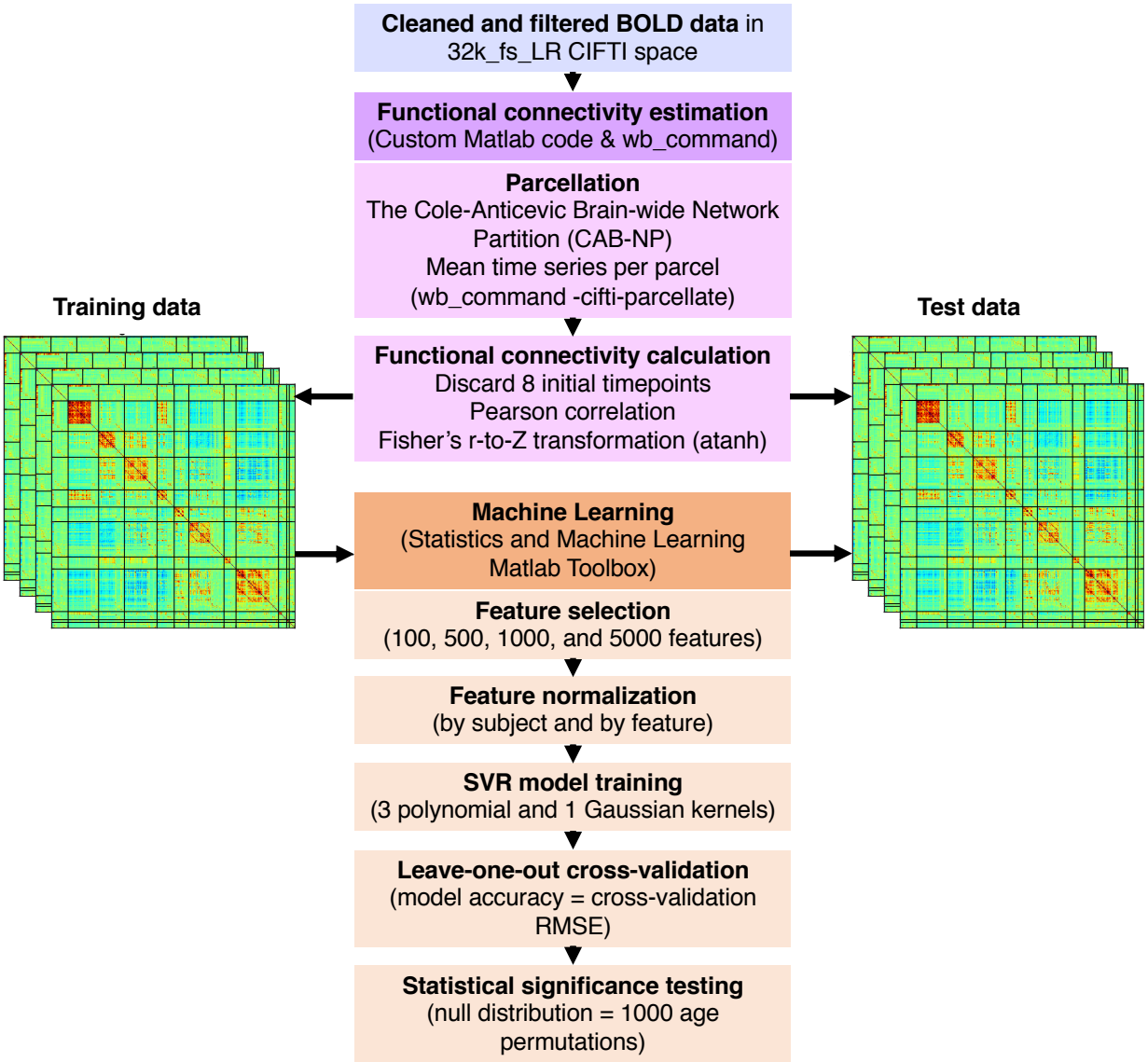

Figure S8. Overview of the functional connectivity estimation and machine learning workflows.

We trained several machine learning algorithms on the training dataset using different numbers of features (i.e., edges or functional connections) and selected the model that had the lowest leave-one-out cross-validation prediction error (see Table S1 for prediction accuracy of different models). We combined the cingulo-opercular and orbito-affective networks into a single network cluster ("affective networks") and trained a normative model of affective network maturation by selecting features from that network cluster.

Feature selection. We trained the affective network functional maturation model on 100, 500, 1000, and 5000 features that showed the strongest absolute correlation with age. Features that were correlated with head motion were excluded. We used leave-one-out cross-validation to determine the optimal number of features based on the lowest cross-validation root-mean-square error (RMSE). Features were normalized within each participant (i.e., converted to z-scores) and then normalized by the mean and standard deviation of the training dataset (i.e., for each feature, we subtracted the group mean and divided by the group standard deviation).

Support vector regression. We used support vector regression (SVR; Drucker et al., 1997; Smola and Schölkopf, 2004; Vapnik, 1995) to train the normative model of affective network functional maturity using the four sets of selected features. SVR is a machine learning algorithm that represents each participant's functional connectivity matrix as a point in multidimensional space (i.e., hyperspace) and fits a linear model to the data in hyperspace. SVR is well-suited for high-dimensional data, such the functional connectome, which consists of over 100,000 unique connections. In contrast to multiple regression, SVR capitalizes on the rich and complex information contained in the functional connectome matrix without running the risk of multicollinearity and loss of degrees of freedom. We used linear epsilon-insensitive SVR implemented in Matlab's Statistics and Machine Learning Toolbox.

The performance of the SVR model can be controlled by two main parameters: epsilon and the C-parameter (e.g., Smola and Schölkopf, 2004). Epsilon defines the size of a tube around the regression line in hyperspace, within which data points that deviate from the regression line carry no penalty. The C-parameter controls the penalty imposed on data points outside of the epsilon-defined tube and helps to prevent overfitting. Thus, the C-parameter defines the trade-off between the flatness of the regression line and tolerance of data points that deviate from it beyond the epsilon margin, such that a larger C allows for a steeper regression line. The loss function is estimated based on each data point's deviation from the epsilon-defined boundary. Smaller epsilon and larger C result in a more flexible model, which is more susceptible to overfitting.

Given that SVR fits a linear model in hyperspace, non-linear relationships between predictor and outcome variables can be tested using the "kernel trick", which transforms nonlinear input data into a higher-dimension feature space, where a linear model can be fitted (e.g., Ben-Hur et al., 2008). Commonly used kernels include polynomial kernels and Gaussian kernels, where the polynomial degree and the sigma control the flexibility of the two kernels, respectively. A larger polynomial degree and smaller sigma are associated with higher risk of overfitting (e.g., Ben-Hur et al., 2008). We trained four SVR models using four different kernels: linear kernel SVR, quadratic kernel SVR, cubic kernel SVR, and Gaussian kernel SVR (sigma = 130). For all the SVR models, we used the following parameters: epsilon = 1.45, C-parameter = 14.5, which were determined using a heuristic procedure in Matlab and yielded optimal performance.

To determine the accuracy of each SVR model trained on four different sets of features (100, 500, 1000, and 5000), we performed leave-one-out cross-validation (LOOCV). Each participant was excluded from the training sample one at a time, and the model was trained on the remaining participants. The held-out participant was then used to test the model. This

procedure was repeated for each participant in the training dataset. In selecting the best performing model, we used the following criteria: lowest LOOCV RMSE, largest LOOCV R^2, lowest number of features, and simplest kernel. Optimal prediction accuracy was achieved with the linear kernel SVR trained on 500 features (see Table S1).

Significance testing of model accuracy. To determine whether the predictive performance of the selected model was statistically different from chance, we used permutation testing. We generated the null distribution by randomly permuting age labels of the training dataset 1000 times and re-trained the model on the permuted data. The statistical significance of the model was determined as the proportion of times a permuted model generated a cross-validation RMSE less than or equal to that of a model trained on true age labels. The selected linear kernel SVR model trained on 500 features was statistically significant at $p < 0.001$.

Control models. Given that head motion is associated with both age and functional connectivity, we tested whether the SVR model's performance was driven by age-related differences in head motion. We trained the SVR model to predict individual framewise displacement (FD) using the same parameters and features as were used to predict age. We then tested the statistical significance of the FD-predicting model using 1000 permutations to build the null distribution. The model trained to predict FD was not statistically significant (RMSE = 0.11, R^2 = 0.21, p = 0.99), suggesting that the predictive performance of the age-predicting model of functional brain maturation was not driven by age-related differences in head motion.

Table S1. Cross-validation root-mean-square errors (RMSE) and R^2 for each of the trained models. The model that was selected as the final normative model is highlighted with a box.

Functional maturity model	**Number of selected features**			
RMSE	**100**	**500**	**1000**	**5000**
Linear kernel SVR	5.06	**4.56**	4.77	5.57
Quadratic kernel SVR	5.18	4.64	4.86	5.84
Cubic kernel SVR	5.37	4.91	5.16	6.29
Gaussian kernel SVR	11.1	7.98	6.8	6.42
R^2	**100**	**500**	**1000**	**5000**
Linear kernel SVR	0.81	**0.86**	0.85	0.82
Quadratic kernel SVR	0.81	0.86	0.85	0.81
Cubic kernel SVR	0.8	0.85	0.85	0.81
Gaussian kernel SVR	0.59	0.82	0.82	0.8

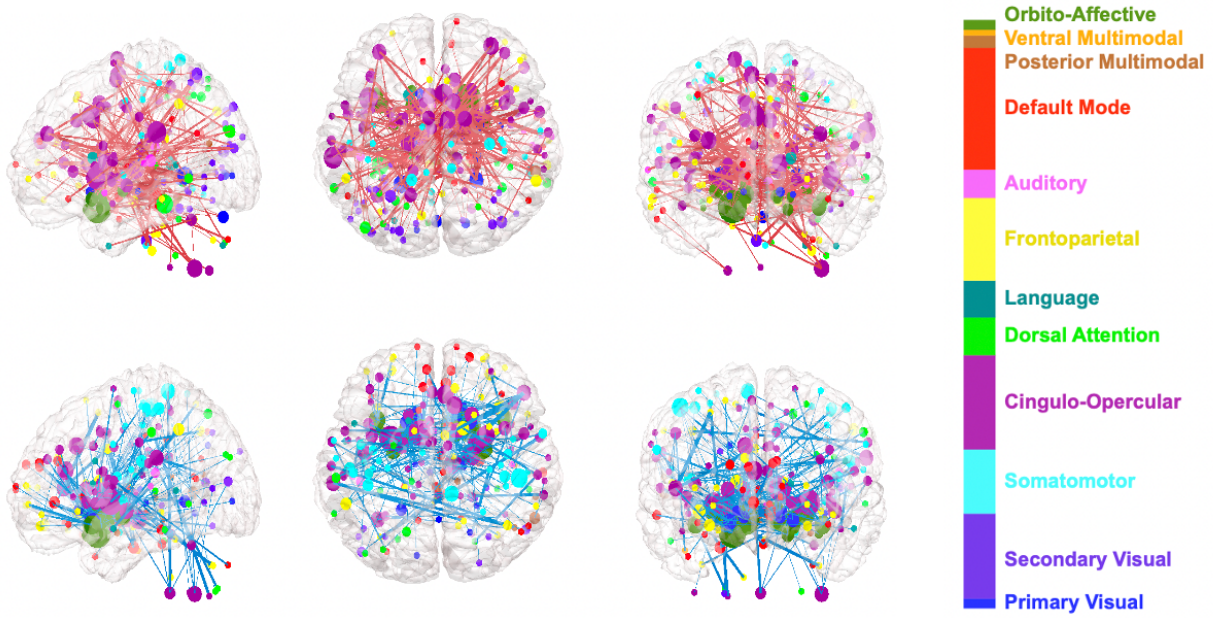

Figure S9. Functional connections with the greatest positive (top panel) and negative (bottom panel) SVR weights (n = 500). Lines represent functional connections (i.e., red lines = positive edges; blue lines = negative edges). Line width is proportional to absolute SVR weights. Circles represent ROIs. Circle size is proportional to the number of positive or negative edges a given ROI forms. Circle color denotes one of the 12 CAB-NP functional networks.

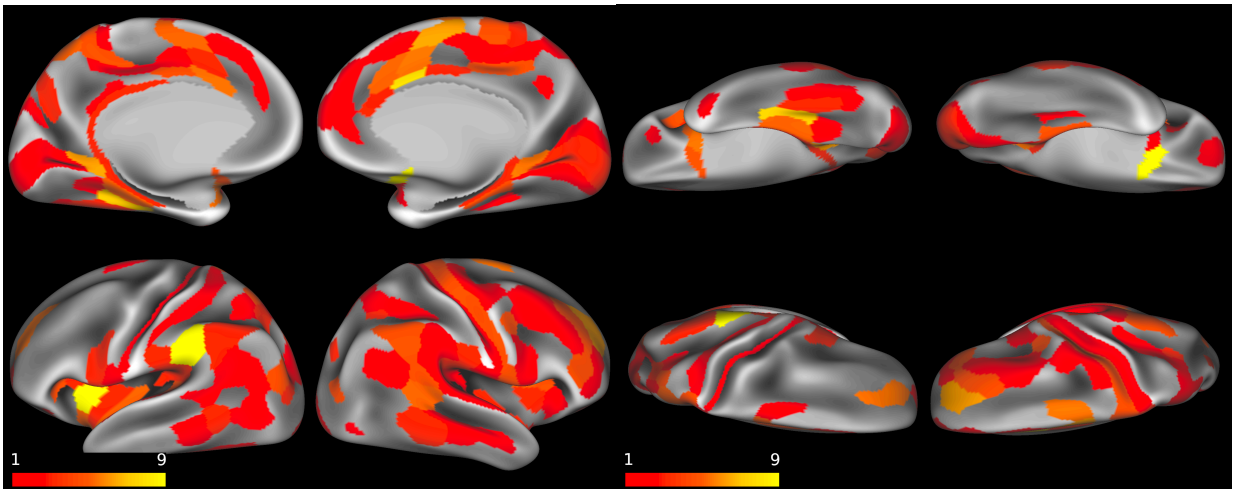

Figure S10. ROIs whose connectivity with other ROIs was positively associated with age. Color denotes number of positive edges a given ROI makes.

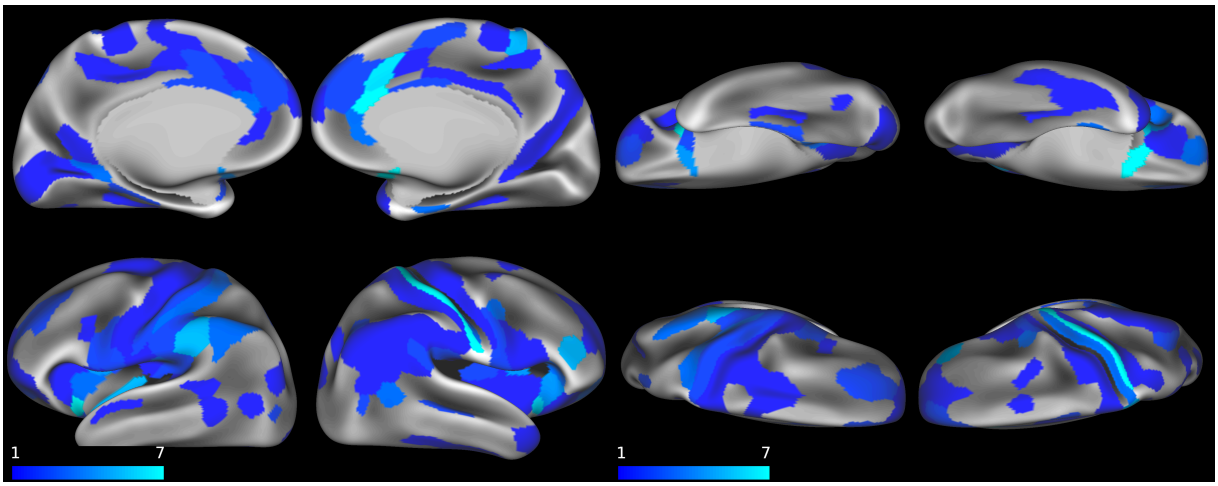

Figure S11. ROIs whose connectivity with other ROIs was negatively associated with age. Color denotes number of negative edges a given ROI makes.

References

Avants, B. B., Epstein, C. L., Grossman, M., & Gee, J. C. (2008). Symmetric diffeomorphic image registration with cross-correlation: Evaluating automated labeling of elderly and neurodegenerative brain. *Medical Image Analysis, 12*(1), 26-41. https://doi.org/10.1016/j.media.2007.06.004

Ben-Hur, A., Ong, C. S., Sonnenburg, S., Schölkopf, B., & Rätsch, G. (2008). Support vector machines and kernels for computational biology. *PLoS Computational Biology, 4*(10), 1-10. https://doi.org/10.1371/journal.pcbi.1000173

Burgess, G. C., Kandala, S., Nolan, D., Laumann, T. O., Power, J. D., Adeyemo, B., ... & Barch, D. M. (2016). Evaluation of denoising strategies to address motion-correlated artifacts in resting-state functional magnetic resonance imaging data from the human connectome project. *Brain Connectivity, 6*(9), 669-680. https://doi.org/10.1089/brain.2016.0435

Ciric, R., Wolf, D. H., Power, J. D., Roalf, D. R., Baum, G. L., Ruparel, K., ... & Gur, R. C. (2017). Benchmarking of participant-level confound regression strategies for the control of motion artifact in studies of functional connectivity. *NeuroImage, 154*, 174-187. https://doi.org/10.1016/j.neuroimage.2017.03.020

Coalson, T. S., Van Essen, D. C., & Glasser, M. F. (2018). The impact of traditional neuroimaging methods on the spatial localization of cortical areas. *Proceedings of the National Academy of Sciences, 115*(27), E6356-E6365. https://doi.org/10.1073/pnas.1801582115

Dale, A. M., Fischl, B., & Sereno, M. I. (1999). Cortical surface-based analysis: I. Segmentation and surface reconstruction. *NeuroImage, 9*(2), 179-194. https://doi.org/10.1006/nimg.1998.0395

Dickie, E. W., Anticevic, A., Smith, D. E., Coalson, T. S., Manogaran, M., Calarco, N., ... & Voineskos, A. N. (2019). Ciftify: A framework for surface-based analysis of legacy MR acquisitions. *NeuroImage, 197*, 818-826. https://doi.org/10.1016/j.neuroimage.2019.04.078

Drucker, H., Burges, C. J., Kaufman, L., Smola, A. J., & Vapnik, V. (1997). Support vector regression machines. In *Advances in Neural Information Processing Systems* (pp. 155-161).

Esteban, O., Markiewicz, C. J., Blair, R. W., Moodie, C. A., Isik, A. I., Erramuzpe, A., ... & Oya, H. (2019). fMRIPrep: A robust preprocessing pipeline for functional MRI. *Nature Methods, 16*(1), 111-116. https://doi.org/10.1038/s41592-018-0235-4

Fonov, V. S., Evans, A. C., McKinstry, R. C., Almli, C. R., & Collins, D. L. (2009). Unbiased nonlinear average age-appropriate brain templates from birth to adulthood. *NeuroImage, 47*, S102. https://doi.org/10.1016/S1053-8119(09)70884-5

Glasser, M. F., Coalson, T. S., Robinson, E. C., Hacker, C. D., Harwell, J., Yacoub, E., ... & Smith, S. M. (2016). A multi-modal parcellation of human cerebral cortex. *Nature, 536*, 171-178. https://doi.org/10.1038/nature18933

Glasser, M. F., Sotiropoulos, S. N., Wilson, J. A., Coalson, T. S., Fischl, B., Andersson, J. L., ... & Van Essen, D. C. (2013). The minimal preprocessing pipelines for the Human Connectome Project. *NeuroImage, 80*, 105-124. https://doi.org/10.1016/j.neuroimage.2013.04.127

Gorgolewski, K., Burns, C. D., Madison, C., Clark, D., Halchenko, Y. O., Waskom, M. L., & Ghosh, S. S. (2011). Nipype: A flexible, lightweight and extensible neuroimaging data processing framework in python. *Frontiers in Neuroinformatics, 5*, 13. https://doi.org/10.3389/fninf.2011.00013

Greve, D. N., & Fischl, B. (2009). Accurate and robust brain image alignment using boundary-based registration. *NeuroImage, 48*(1), 63-72. https://doi.org/10.1016/j.neuroimage.2009.06.060

Huntenburg, J. M. (2014). *Evaluating nonlinear coregistration of BOLD EPI and T1w images* [Doctoral dissertation, Freie Universität Berlin]. Available from: http://hdl.handle.net/11858/00-001M-0000-002B-1CB5-A.

Jenkinson, M., Bannister, P., Brady, M., & Smith, S. (2002). Improved optimization for the robust and accurate linear registration and motion correction of brain images. *NeuroImage, 17*(2), 825-841. https://doi.org/10.1006/nimg.2002.1132

Ji, J. L., Spronk, M., Kulkarni, K., Repovš, G., Anticevic, A., & Cole, M. W. (2019). Mapping the human brain's cortical-subcortical functional network organization. *NeuroImage, 185*, 35-57. https://doi.org/10.1016/j.neuroimage.2018.10.006

Klein, A., Ghosh, S. S., Bao, F. S., Giard, J., Häme, Y., Stavsky, E., ... & Keshavan, A. (2017). Mindboggling morphometry of human brains. *PLoS Computational Biology, 13*(2). https://doi.org/10.1371/journal.pcbi.1005350

Lanczos, C. (1964). Evaluation of noisy data. *Journal of the Society for Industrial and Applied Mathematics, Series B: Numerical Analysis, 1*(1), 76-85. https://doi.org/10.1137/0701007

Parkes, L., Fulcher, B., Yücel, M., & Fornito, A. (2018). An evaluation of the efficacy, reliability, and sensitivity of motion correction strategies for resting-state functional MRI. *NeuroImage, 171*, 415-436. https://doi.org/10.1016/j.neuroimage.2017.12.073

Power, J. D., Barnes, K. A., Snyder, A. Z., Schlaggar, B. L., & Petersen, S. E. (2012). Spurious but systematic correlations in functional connectivity MRI networks arise from subject motion. *NeuroImage, 59*(3), 2142-2154. https://doi.org/10.1016/j.neuroimage.2011.10.018

Power, J. D., Mitra, A., Laumann, T. O., Snyder, A. Z., Schlaggar, B. L., & Petersen, S. E. (2014). Methods to detect, characterize, and remove motion artifact in resting state fMRI. *NeuroImage, 84,* 320-341. https://doi.org/10.1016/j.neuroimage.2013.08.048

Robinson, E. C., Garcia, K., Glasser, M. F., Chen, Z., Coalson, T. S., Makropoulos, A., ... & Hutter, J. (2018). Multimodal surface matching with higher-order smoothness constraints. *NeuroImage, 167*, 453-465. https://doi.org/10.1016/j.neuroimage.2017.10.037

Satterthwaite, T. D., Elliott, M. A., Gerraty, R. T., Ruparel, K., Loughead, J., Calkins, M. E., ... & Wolf, D. H. (2013a). An improved framework for confound regression and filtering for control of motion artifact in the preprocessing of resting-state functional connectivity data. *NeuroImage, 64*, 240-256. https://doi.org/10.1016/j.neuroimage.2012.08.052

Smola, A. J., & Schölkopf, B. (2004). A tutorial on support vector regression. *Statistics and Computing, 14*(3), 199-222. https://doi.org/10.1023/B:STCO.0000035301.49549.88

Smyser, C. D., Inder, T. E., Shimony, J. S., Hill, J. E., Degnan, A. J., Snyder, A. Z., & Neil, J. J. (2010). Longitudinal analysis of neural network development in preterm infants. *Cerebral Cortex, 20*(12), 2852-2862. https://doi.org/10.1093/cercor/bhq035

Treiber, J. M., White, N. S., Steed, T. C., Bartsch, H., Holland, D., Farid, N., ... & Chen, C. C. (2016). Characterization and correction of geometric distortions in 814 diffusion weighted images. *PloS One, 11*(3), e0152472. https://doi.org/10.1371/journal.pone.0152472

Tustison, N. J., Avants, B. B., Cook, P. A., Zheng, Y., Egan, A., Yushkevich, P. A., & Gee, J. C. (2010). N4ITK: Improved N3 bias correction. *IEEE Transactions on Medical Imaging, 29*(6), 1310-1320. https://doi.org/10.1109/TMI.2010.2046908

Vapnik, V. N. (1995). The nature of statistical learning theory. Springer, New York, 1995.

Zhang, Y., Brady, M., & Smith, S. (2001). Segmentation of brain MR images through a hidden Markov random field model and the expectation-maximization algorithm. *IEEE Transactions on Medical Imaging, 20*(1), 45-57. https://doi.org/10.1109/42.906424